Auger decay of the C $1s \rightarrow 2\pi^*$ excitation of CO

Shaleen K. Botting and Robert R. Lucchese
Department of Chemistry, Texas A&M University, College Station, Texas 77843-3255
(Received 5 June 1997)

Calculations on the Auger decay of CO after the C $1s \rightarrow 2\pi^*$ excitation have been performed utilizing a multichannel Schwinger approach. The bound orbitals used to expand the multichannel configuration-interaction wave functions of the ion state were the natural orbitals of a single excitation and double excitation configuration-interaction (CI) calculation on the C $1s^{-1}$ core-hole state of CO. Fixed-nuclei photoionization cross sections were then obtained with target states represented by complete active space CI wave functions. An analysis of the resulting cross sections using Fano's spectral line profile and the lifetime vibrational interference theory has lead to photoabsorption profiles in good agreement with experimental measurements. Additionally, we have found good agreement with experimental data for the resulting photoelectron and photoemission spectra. [S1050-2947(97)00511-8]

PACS number(s): 33.80.Eh, 33.60.Fy, 33.70.−w

I. INTRODUCTION

The advent of synchrotron radiation sources and the subsequent improved experimental studies on molecular photoionization processes [1–3] have stimulated a corresponding development of theoretical methods for studying electron-molecule scattering [4–7]. In the past decade, experimental data resulting from improvements in monochromator resolution now allow detailed study of the short-lived nature of the electronic deexcitation leading to the Auger spectra of diatomic molecules such as carbon monoxide (CO) [8]. These high-resolution experimental studies provide the possibility for a comparison with computed spectral functions, which was not available previously due to the extremely small spectral linewidth necessary to separate the individual decay channels. In this study we considered the excitation and decay of the C $1s \rightarrow 2\pi^*$ resonance state in CO obtained by the excitation of the CO molecule with photons of an energy of approximately 287.5 eV.

Autoionization is the process where the photoabsorption excitation energy is sufficiently energetic to excite a resonance state in which one of the electrons has been excited into a bound valance orbital and is moving in the field of an excited ionic state. This excited resonance state then decays into a continuum electron and a lower-energy ionic state. The C $1s \rightarrow 2\pi^*$ resonance state in CO occurs at an energy slightly below the energy of the core-hole ion state and the $2\pi^*$ electron moves in the field of the ion state, which is very similar to the C $1s^{-1}$ core-hole state of CO. The resonance state is usually only weakly coupled to the continuum, which leads to a long lifetime for the resonance state.

There are two possible forms of decay in the autoionization process: participator and spectator. A spectator type decay is a transition from a one-hole–one-particle excited state to a two-hole–one-particle final state, whereas a participator-type decay occurs from an excited state that is similar to that found in the spectator decay but decays to a one-hole final state. Typically, only the one-hole final states are detected experimentally. Consequently, the autoionization process from the C $1s \rightarrow 2\pi^*$ excitation of CO is commonly and misleadingly referred to as a participator Auger decay. However, we will see from our study that there are numerous pathways for the relaxation of the C $1s \rightarrow 2\pi^*$ resonance state and that the decay into two-hole–one-particle shake-up states is quite significant. Thus we will demonstrate that the process by which CO decays is both participator and spectator in nature.

The body of this work is an extension of an earlier core-ionization study [9] that includes the computation of photoionization cross sections of highly excited core-hole states for the diatomic molecule CO. CO is one of the simplest heteroatomic diatomics, chosen here because it not only provides enough complexity to be interesting, but has few enough electrons to be amenable to more extensive quantum-mechanical calculations. With our calculations we have provided some additional insight into the branching ratios of the individual channels as well as clarified some ambiguity in the experimental assignment of electronic deexcitation spectral peaks.

The rest of the paper is organized as follows. Section II briefly discusses the theory. The computational details are given in Sec. III. Section IV is devoted to the results and discussion and is further divided into three subsections. Section IV A focuses on the results of this study employing the fixed-nuclei approximation in the calculation of the photoabsorption cross sections of core-hole excited states of CO, including the application of Fano's [10] line profile in the analysis of the resonance line shapes. In Sec. IV B the theoretical simulation of both the radiative and nonradiative decay spectra is presented. In Sec. IV C the lifetime-vibrational interference theory is applied to the theoretical simulation of the photoabsorption spectrum for the C $1s \rightarrow 2\pi^*$ absorption of CO. Conclusions to this study are in Sec. V.

II. THEORY

The method employed in all the scattering calculations in this photoionization study is a multichannel Schwinger approach with Padé approximant corrections [4–6]. The multichannel configuration-interaction (MCCI) wave function for a system with a continuum electron is written as

$$\Psi_{\mathrm{MCCI}}=\sum_{i=1}^{N_c}\Phi_i(\xi_i)=\sum_{i=1}^{N_c}\sum_{j=1}^{N_b}C_{ij}\psi_j(\xi_i), \tag{1}$$

where ξ_i is the ith channel scattering state and Φ_i represents the configuration-interaction (CI) wave function of the residual ion in channel i. N_c is the number of channels and N_b is the number of configuration state functions (CSFs) in the expansion. The notation $\psi_j(\xi_i)$ implies a spin-adapted N-electron CSF, not a simple product of ψ_j and ξ_i.

To obtain the equations for the scattering orbital ξ_i, the MCCI wave function given above is required to satisfy the projected Schrödinger equation

$$\left\langle \sum_{i=1}^{N_c}\Phi_i(\delta\xi_i)\middle|\mathcal{H}_{\mathrm{el}}-E\middle|\Psi_{\mathrm{MCCI}}\right\rangle=0, \tag{2}$$

where $\mathcal{H}_{\mathrm{el}}$ is the purely electronic Hamiltonian and the bra represents all possible variations of $\Phi_i(\xi_i)$ that may be obtained by the variation of the scattering orbital. The derivation of the form of the scattering potential is covered in detail by Bandarage and Lucchese [9] and its evaluation is discussed by Stratman and Lucchese [11]. If the formalism described above is applied to photoionization then the channel transition monent may be obtained, where final variational expression for the channel transition moment $I_i^{L(V)}$ is given by

$$I_i^{L(V)}=\langle R_i^{L(V)}|\xi_i^0\rangle+\sum_{\alpha,\beta}\langle R_i^{L(V)}|\underline{G}_c\underline{V}_Q|\phi_\alpha''\rangle \times\langle \underline{V}_Q-\underline{V}_Q\underline{G}_c\underline{V}_Q\rangle^{-1}_{\alpha\beta}\langle\phi_\beta''|\underline{V}_Q|\xi_i^0\rangle, \tag{3}$$

where the quantity $R_i^{L(V)}$ is a function of the electronic dipole operator $\mu_i^{L(V)}$. The superscript $L(V)$ denotes that this equation may be solved either for the length form or for the velocity form, which differ by the value of the electronic dipole operator represented by

$$\mu_i^L(j)=\sqrt{k_i}\mathbf{r}_j\cdot\hat{\mathbf{n}} \tag{4}$$

and

$$\mu_i^V(j)=(\sqrt{k_i}/\hbar\omega)\boldsymbol{\nabla}_j\cdot\hat{\mathbf{n}} \tag{5}$$

in the length and velocity forms, respectively, where $\hat{\mathbf{n}}$ is the direction of the polarization of the light, ω the frequency of the photon, and k_i the momentum of the photoelectron in the ith channel. $\underline{V}_Q$ in Eq. (3) is the Phillips-Kleinman pseudopotential [9] and $\underline{G}_c$ is the multichannel Coulomb Green's function matrix given by

$$(\underline{G}_c)_{ij}=G_c(E_i)\delta_{ij}, \tag{6}$$

where the Coulomb Green's function is defined as

$$\left(-\frac{1}{2}\nabla^2-\frac{1}{r}-E_i\right)G_c(\mathbf{r},\mathbf{r}')=-\delta^3(\mathbf{r}-\mathbf{r}'). \tag{7}$$

In the mixed form the doubly differential photoionization cross section of a given channel is proportional to the product of the length and velocity forms of transition moments from Eq. (3) and is given by

$$\frac{d^2\sigma^M}{d\Omega_{\hat{\mathbf{k}}_i}d\Omega_{\hat{\mathbf{n}}}}=\frac{4\pi^2\hbar\omega}{c}\,\mathrm{Re}\{(I_i^L)^*I_i^V\}. \tag{8}$$

The final equation for the differential cross section is obtained by integrating Eq. (8) over all spatial orientations of the molecule in the laboratory frame.

Fano's [10] theory treats the phenomenon of autoionization both in the case where one discrete state and one continuum of states mix and in the case where more than one continuum interacts with the discrete state. In the case where there is one discrete state and one continuum, Fano's final profile to fit the transition probability is given in terms of the transition dipole matrix operator T or the transition probability. This profile is given by

$$\frac{|\langle\Psi_E|T|i\rangle|^2}{|\langle\psi_E|T|i\rangle|^2}=\frac{(q+\varepsilon)^2}{1+\varepsilon^2}, \tag{9}$$

where the left-hand side of the equation is the ratio of the transition probability from the initial state $|i\rangle$ to the true final state $|\Psi_E\rangle$ to the probability of a transition to the unperturbed continuum state $|\psi_E\rangle$. The reduced energy variable ε and the quantity q on the right-hand side of Eq. (9) are determined by the equations

$$q^2=\frac{\langle\varphi|T|i\rangle}{\langle\psi_E|T|i\rangle\frac{1}{2}\pi\Gamma} \tag{10}$$

and

$$\varepsilon=\frac{E-[E_\varphi+F(E)]}{\frac{1}{2}\Gamma}, \tag{11}$$

where $|\varphi\rangle$ represents the resonance state, Γ is the spectral linewidth, $E_\varphi+F(E)$ represents the energy of the resonance, and E is the excitation energy.

Cross sections and their related spectral intensities are greatly influenced by the dynamics of both the intermediate state and the final state. If the intermediate state is long lived, the absorption intensity will have a series of sharp resonance peaks exhibiting the vibrational spacing of a system where the intensity is predominately governed by the Franck-Condon principle and the excitation-decay process can be described as two independent steps. The first step, the initial excitation of the electron from the ground state to the intermediate state, results in a population distribution represented by the Franck-Condon matrix elements. The second step, in which the intermediate decays, is practically independent of the first excitation step, thus it may also be described by the Franck-Condon matrix elements. Therefore, the observed intensity $\mathcal{I}$ of the transition between the initial and the final state going through a particular intermediate state $|n\rangle$ may be given by [1]

$$\mathcal{I}\propto|\langle I|T|F\rangle|^2=|M_{In}|^2|M_{nF}|^2|\langle I|n\rangle|^2|\langle n|F\rangle|^2, \tag{12}$$

where $\langle I|n\rangle$ and $\langle n|F\rangle$ are the vibrational overlap integrals of the wave functions for the initial state I, intermediate state n, and final state F, and the electronic transition matrix elements are represented by M_{In} and M_{nF}. Equation (12) is valid as long as the peaks are very narrow and are adequately

separated. However, when the lifetime of the intermediate state is so short that lifetime broadening results in overlapping of the vibrational levels, the decay spectrum becomes more complicated as both constructive and destructive interference modify the spectrum.

There have been numerous theoretical descriptions of the vibrational structure of the photoabsorption spectra of small molecules. For molecules with a decay time on the order of their vibrational frequency, it is widely known that interference is observed in the vibronic emission spectra. The expression used to calculate the spectral intensity $\mathcal{I}$ is

$$\mathcal{I} \propto |\langle I|T|F\rangle|^2 = \left| \sum_n \frac{M_{In}\langle I|n\rangle\langle n|F\rangle M_{nF}}{E - E_n' - \frac{1}{2}i\Gamma} \right|^2, \qquad (13)$$

where E is the excitation energy, E_n' is the energy difference between the initial state and the nth vibrational energy level in the intermediate state, T is the transition dipole operator, and Γ is the spectral linewidth.

III. COMPUTATIONS

The photoionization cross-section calculations were performed in two major stages beginning with the calculation of a set of natural orbitals. These molecular orbitals were generated by performing a Hartree-Fock (HF) calculation on the core-hole state of CO^+ utilizing the GAMESS-UK [12] computer code. This is done by first performing a restricted Hartree-Fock calculation on the electronic ground state of CO $(1\sigma)^2(2\sigma)^2(3\sigma)^2(4\sigma)^2(1\pi)^4(5\sigma)^2$ at the equilibrium internuclear distance of 2.132 a.u. [13] using a standard triple ζ valence plus polarization basis set augmented by a set of diffuse functions. We included the diffuse functions to describe the first two Rydberg orbitals of CO [14]. The resulting ground-state energy for CO is $-112.775\,974$ a.u. This calculation yielded a set of molecular orbitals that were used in the subsequent restricted open-shell HF calculation on the core-hole state of CO^+, with a final total energy of $-101.842\,717$ a.u. The final step to acquire the needed natural orbitals for the scattering calculation again utilized the GAMESS-UK program, this time to perform a CI on the core-hole state, freezing the 1σ orbital and using 36 virtual orbitals, resulting in a total CI energy for the core-hole state of $-101.916\,624$ a.u.

The second step of the calculations leading to the scattering cross sections utilized the ten orbitals with the highest occupation from the natural orbital set generated using GAMESS-UK. The transition moments defined in Eq. (3) are numerically determined using a single-center expansion. This technique is discussed in detail elsewhere [5] and will not be covered in this work. The radial grid used in this study contained a maximum of 3500 points. As in previous studies [15], we found that the differences between energies of the various ion states obtained were relatively insensitive to the maximum value of l, used in the partial-wave expansion. Here we used a value of $l_m = 60$.

Calculation of the cross sections was performed in two different fashions. The first will be referred to as a ''two-channel'' calculation. In these calculations a multichannel calculation was performed including the core-hole channel and an individual valence ion channel. The second method was to perform a ''five-channel'' calculation. This included a valence ion state, the C $1s$ core-hole state, and three ion shake-up states above the core-hole state. A shake-up (SU) state differs from the core-hole state by a single electron excitation. The addition of the shake-up states allowed for the inclusion of correlation effects in the description of the resonance state. The SU ion states included in the calculation were selected using the following procedure.

TABLE I. Shake-up and core-hole states of CO^+ and their ionization potentials.

State	IP (eV)	Principal configuration
core hole	287.04	$1\sigma^2 2\sigma^1 3\sigma^2 4\sigma^2 5\sigma^2 1\pi^4 2\pi^0$
586 $^2\Sigma$	297.94	$1\sigma^2 2\sigma^1 3\sigma^2 4\sigma^2 5\sigma^2 1\pi^3 2\pi^1$
486 $^2\Pi$	294.94	$1\sigma^2 2\sigma^1 3\sigma^2 4\sigma^2 5\sigma^1 1\pi^4 2\pi^1$
284 $^2\Delta$	310.71	$1\sigma^2 2\sigma^1 3\sigma^2 4\sigma^2 5\sigma^2 1\pi^2 2\pi^2$

First an approximate description of the resonance state was obtained by diagonalizing the $14e^-$ complete active space CI Hamiltonian. The next step was to find the overlap integral of this approximate C $1s \rightarrow 2\pi^*$ resonance state with penetration terms [15] constructed from various shake-up states. A penetration term is an N-electron CI wave function constructed by taking the spin-adapted antisymmetrized product of a target molecular orbital and a CI wave function for an $(N-1)$-electron ion target state. By performing all possible combinations of states, three shake-up states were finally chosen whose penetration terms had a total overlap integral with the resonance state of 0.994. These three states are listed in Table I along with their ionization potentials. We found that the peak energy at the maximum shifted from 280.303 to 279.154 eV for the two- and five-channel calculations, respectively. This decrease in the energy of the peak maximum for the resonance state of 1.15 eV can be attributed to the inclusion of correlation.

The Schwinger-method-with-Páde-approximants study of the photoionization cross sections for the C $1s \rightarrow 2\pi^*$ excitation of CO yielded information for various possible final ion state channels. To choose the final valence ion state channels to use in this study, all valance ion configurations were identified that could be obtained from two-electron Auger decay process from the resonant $1\sigma^2 2\sigma^1 3\sigma^2 4\sigma^2 5\sigma^2 1\pi^4 2\pi^1$ configuration. Then the valance ion states that had a greater than 50% contribution from one of the identified configurations were selected. This resulted in a set of 31 channels chosen from the $^2\Sigma, ^2\Pi, ^2\Delta$ symmetries. The cross section for each possible channel was computed at a sufficient number of energies to adequately describe the structure of the resonant peak.

IV. RESULTS AND DISCUSSION

A. Fixed-nuclei approximation

The computed fixed-nuclei resonance absorption profiles were analyzed by fitting the computed cross sections to the Fano absorption profile given in Eq. (9). Fano's profile provided an excellent fit to the resonance peaks. From this fit we were able to obtain the peak maximum, the decay width Γ of the autoionizing state, and the transition dipole moment

TABLE II. Computed ionization potentials (IPs) of the states of CO^+ and partial decay widths to the ion state from the C $1s \rightarrow 2\pi^*$ resonance state.

Principal configuration	Symmetry	IP (eV)	Width (meV) 2C	5C
$(4\sigma)^{-1}(5\sigma)^{-1}(2\pi)^{+1}$	$^2\Pi$	22.6	15.9	12.5
$(1\pi)^{-1}$	$^2\Pi$	12.6	9.8	9.8
$(5\sigma)^{-2}(2\pi)^{+1}$	$^2\Pi$	17.6	4.6	4.8
$(5\sigma)^{-1}(3\sigma)^{-1}(2\pi)^{+1}$	$^2\Pi$	41.5	4.6	4.0
$(5\sigma)^{-1}(1\pi)^{-1}(2\pi)^{+1}$	$^2\Delta$	20.7	4.5	3.8
$(4\sigma)^{-1}(5\sigma)^{-1}(2\pi)^{+1}$	$^2\Pi$	23.9	4.2	3.7
$(5\sigma)^{-1}(1\pi)^{-1}(2\pi)^{+1}$	$^2\Sigma$	19.2	4.2	3.5
$(5\sigma)^{-1}(1\pi)^{-1}(2\pi)^{+1}$	$^2\Delta$	17.8	3.5	2.8
$(5\sigma)^{-1}$	$^2\Sigma$	8.5	3.1	2.9
$(5\sigma)^{-1}(1\pi)^{-1}(2\pi)^{+1}$	$^2\Sigma$	21.2	2.5	2.2
$(4\sigma)^{-1}$	$^2\Sigma$	15.3	2.0	2.0
$(5\sigma)^{-1}(1\pi)^{-1}(2\pi)^{+1}$	$^2\Sigma$	17.7	1.3	1.0
$(4\sigma)^{-1}(1\pi)^{-1}(2\pi)^{+1}$	$^2\Delta$	28.1	1.0	1.0
$(3\sigma)^{-1}$	$^2\Sigma$	33.9	0.7	0.9
$(3\sigma)^{-1}(1\pi)^{-1}(2\pi)^{+1}$	$^2\Delta$	45.7	0.8	0.8
$(4\sigma)^{-1}(1\pi)^{-1}(2\pi)^{+1}$	$^2\Sigma$	30.1	0.8	0.7
$(5\sigma)^{-1}(1\pi)^{-1}(2\pi)^{+1}$	$^2\Sigma$	45.8	0.6	0.6
$(4\sigma)^{-1}(1\pi)^{-1}(2\pi)^{+1}$	$^2\Sigma$	28.4	0.5	0.5
Total width			64.6	60.0

$|\langle\varphi|T|i\rangle|^2$. A fit was performed for each chosen channel. The resulting partial decay widths are tabulated in Table II in decreasing order of widths in the five-channel calculation, along with the principal configuration, ionization potential, and symmetry of each state. While all 31 channels were considered, only those with a decay width greater then 0.5 meV are included in the table. As discussed in Sec. III, all calculations were performed both with two channels (2C) and with five channels (5C). Referring back to Table II, we note that the partial decay widths for the five-channel calculation vary slightly from the two-channel widths. The summed width of all 31 calculated channels, referred to here as the total width, is approximately 8% lower for the five-channel calculations. One reason for this difference may be that additional correlation in the resonance state will add configurations that do not have coupling matrix elements with the final states under consideration here at the expense of configurations that do couple with those states. This implies that the decay probability may have increased to some of the weaker final states. A definitive conclusion would require additional studies.

The determination of the radiative lifetime from the resonance state to the ground state is a straightforward extension of fitting the fixed-nuclei cross-section peaks to the mathematical peak profile of Fano. One of the factors obtained from the fitting of Fano's profile was the transition dipole moment $|\langle\varphi|T|i\rangle|^2$. Using the relationship between the transition dipole moment and the lifetime $\tau_{\varphi i}$,

$$\tau_{\varphi i}=\frac{3hc^3}{64\pi^4\nu_{\varphi i}^3|\langle\varphi|T|i\rangle|^2}, \tag{14}$$

TABLE III. Radiative and nonradiative decay partial widths for selected channels from the C $1s \rightarrow 2\pi^*$ resonance state. The radiative widths given are for decay to the $X\ ^1\Sigma^+$ ground state of CO.

Channel	Nonradiative width (meV)	Radiative width (meV)
$(4\sigma)^{-1}(5\sigma)^{-1}(2\pi)^{+1}$	12.5	1.77
$(1\pi)^{-1}$	4.8	1.77
$(5\sigma)^{-1}(1\pi)^{-1}(2\pi)^{+1}$	3.5	1.78
$(3\sigma)^{-1}$	0.8	1.61
$(3\sigma)^{-1}(1\pi)^{-1}(2\pi)^{+1}$	0.7	1.91

the average radiative decay lifetime of the core-hole resonance state using this method was found to be 3.7×10^{-13} s, slightly higher than that predicted by Neeb *et al.* [8] of a ''few'' femtoseconds. From the calculated lifetimes using Eq. (14) and the relationship

$$\Gamma_i \approx \hbar/\tau_i, \tag{15}$$

the radiative decay widths were then calculated. In Table III we see that the calculated radiative decay width for decay from the resonance state to the ground state is nearly independent of which nonradiative channel is being considered. In addition, Table III illustrates, for a few selected channels, that the nonradiative decay widths calculated using Fano's spectral line profile vary significantly for each channel.

Following the logic of Fano's multicontinua problem [10], the sum of the individual partial widths for each channel should be a good approximation to the total observed spectral linewidth. To the extent that this approximation is good, then a very time intensive multichannel computation may be simplified into a series of shorter calculations where only one final ion state is included. To check this additivity approximation, we compared the total width of a small number of channels computed together versus the sum of their widths computed separately. We have found that the two methods of computing the widths agree within 0.2%.

Note that the total width presented in Table II includes only the nonradiative decay pathways. Therefore, our next step was to compute the contribution from the radiative decay to the total width. The determination of the radiative lifetimes from the resonance state to the individual neutral states began with calculation of the oscillator strengths, obtained from the same codes used to calculate the cross sections. The relationship between oscillator strength f and the transition matrix element given in atomic units is given by

$$f=\tfrac{4}{3}\pi\nu_{\varphi i}|\langle\varphi|T|i\rangle|^2. \tag{16}$$

From Eqs. (14)–(16) the radiative decay widths were then calculated. Table IV contains the calculated radiative decay widths greater than 0.005 meV along with the principal configurations and emission energies for the final states. Referring to the first configuration in Table IV, note that this is the radiative decay of the core-hole state given here with a 2.285 meV width. As expected, this width is comparable to the average radiative decay width of 1.758 meV calculated from Fano profile fits displayed in Table III. The slight difference in these two values is due to the fact that the single 2π orbital from the core-hole CI calculation is going to be some-

TABLE IV. Computed radiative decay widths and emission energies to the significant final states from the C $1s \rightarrow 2\pi^*$ resonance state.

Configuration	Symmetry	Energy (eV)	Decay width (meV)
$1\sigma^2 2\sigma^2 3\sigma^2 4\sigma^2 5\sigma^2 1\pi^4$	$1\,^1\Sigma^+$	287.04	2.285
$(5\sigma)^{-1}(1\pi)^{-1}(2\pi)^{+2}$	$1\,^1\Pi$	278.81	0.788
$(1\pi)^{-1}(2\pi)^{+1}$	$1\,^1\Delta$	276.96	0.366
$(1\pi)^{-1}(2\pi)^{+1}$	$3\,^1\Sigma^+$	276.93	0.199
$(5\sigma)^{-2}(2\pi)^{+2}$	$2\,^1\Delta$	271.12	0.014
$(4\sigma)^{-1}(5\sigma)^{-1}(2\pi)^{+2}$	$3\,^1\Delta$	265.18	0.033
$(4\sigma)^{-1}(5\sigma)^{-1}(2\pi)^{+2}$	$6\,^1\Sigma^+$	264.35	0.009
$(4\sigma)^{-1}(1\pi)^{-1}(2\pi)^{+2}$	$5\,^1\Pi$	263.51	0.008
$(1\pi)^{-2}(2\pi)^{+2}$	$4\,^1\Delta$	259.72	0.006
$(1\pi)^{-2}(2\pi)^{+2}$	$9\,^1\Sigma^+$	259.34	0.014
$(1\pi)^{-2}(2\pi)^{+2}$	$5\,^1\Delta$	258.95	0.015
$(5\sigma)^{-1}(1\pi)^{-1}(2\pi)^{+2}$	$6\,^1\Pi$	258.74	0.036
$(1\pi)^{-1}(2\pi)^{+2}$	$7\,^1\Pi$	258.17	0.022
$(1\pi)^{-1}(2\pi)^{+2}$	$9\,^1\Pi$	256.52	0.040
Total width			3.855

what different from the 2π resonant orbital described numerically in the scattering calculation. In the final comparison of the total calculated spectral linewidth with experimental lifetime widths previously published, our results, taking the sum of the radiative and nonradiative decay widths, still fall short of the experimental decay width of the C $1s \rightarrow 2\pi^*$ resonance state as shown in Table V. The deficiency in our calculated final total width has two probable causes. The first probable cause is the use of the core-hole orbitals in the calculation of the CI wave functions used in the Schwinger scattering code. The core-hole orbitals along with the chosen shake-up states provide a reasonable but not exact representation of the resonance state. Second, the total nonradiative decay width reported in Table IV is the sum of the 31 scattering channels calculated. This is only a small sample of the many possible channels, although they were chosen such that they should include all of the main channels. It is possible that decay to the many neglected weak channels, including the continuum of doubly ionized ($N-1$)-electron ion states, could explain the missing decay width.

B. Radiative and nonradiative decay spectra

Using the results of our calculation, we have also simulated experimental spectra for the radiative and nonradiative decay. Under the assumption that the spectral linewidth for a given channel is a good representation of the coupling to the continuum, the ratio of the widths must therefore correspond to the ratio of the decay probabilities. For the nonradiative decay, we assume a Gaussian distribution of the incoming photon energies. The width of the distribution was matched to the observed width the experimental spectrum [16] to account for broadening due to excitation linewidth. The final full width at half maximum (FWHM) of the Gaussian curve was 1.68 eV. This Gaussian curve was weighted with the partial spectral decay width for each channel and then placed at the relative ionization energies as given in Table III. The final calculated spectrum is shown in Fig. 1, as well as the comparable experimental spectrum reported by Eberhardt *et al.* [16]. In this figure our theoretical spectrum was shifted by 7.4 eV to match the energy of the strongest experimental peak at 27.8 eV. This was done because relative ionization potentials are more accurately obtained then are the absolute values. Additionally, the relative experimental data were scaled so that the two spectra agreed at 27.8 eV. Figure 1 shows that our calculations reproduce the intensity pattern of the deexcitation spectrum very well to within 1 eV. Table VI lists our assignments of the visible and underlying peaks in Fig. 1, as well as the corresponding assignments made by

TABLE V. Total radiative and nonradiative decay width from the C $1s \rightarrow 2\pi^*$ resonance state.

Decay width (meV)	Source
63.9	this study
85($\pm$3)	Shaw *et al.*[a]
86($\pm$10)	Osborne *et al.*[b]

[a]Reference [24].
[b]Reference [1].

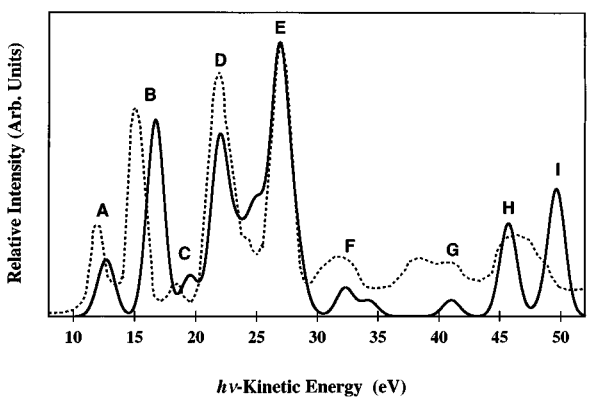

FIG. 1. Deexcitation electron spectra of CO: experimental spectrum from Eberhardt *et al.* [16], ----, and this study, —.

TABLE VI. Dominant configurations for the peaks of the deexcitation spectra as labeled in Fig. 2.

	Configuration	
Peak label	This study	Eberhardt[a]
A	$(5\sigma)^{-1}$	$(5\sigma)^{-1}$
B	$(1\pi)^{-1}$	$(1\pi)^{-1}$
C	$(4\sigma)^{-1}$	$(4\sigma)^{-1}$
D	$(5\sigma)^{-1}(1\pi)^{-1}(2\pi)^{+1}$ $(5\sigma)^{-2}(2\pi)^{+1}$	$(5\sigma)^{-1}(1\pi)^{-1}(2\pi)^{+1}$ $(5\sigma)^{-2}(2\pi)^{+1}$
E	$(4\sigma)^{-1}(5\sigma)^{-1}(2\pi)^{+1}$	$(4\sigma)^{-1}(5\sigma)^{-1}(2\pi)^{+1}$ or $(5\sigma)^{-1}(1\pi)^{-1}(2\pi)^{+1}$
F	$(4\sigma)^{-1}(1\pi)^{-1}(2\pi)^{+1}$	$(4\sigma)^{-1}(1\pi)^{-1}(2\pi)^{+1}$
G	$(3\sigma)^{-1}$	$(3\sigma)^{-1}$
H	$(3\sigma)^{-1}(5\sigma)^{-1}(2\pi)^{+1}$	$(3\sigma)^{-1}(5\sigma)^{-1}(2\pi)^{+1}$
I	$(3\sigma)^{-1}(1\pi)^{-1}(2\pi)^{+1}$ $(5\sigma)^{-2}(1\pi)^{-1}(2\pi)^{+1}$	

[a]Reference [16].

Eberhardt *et al.* Most of Eberhardt's experimental peak assignments are in agreement with our theory; however, we were able to clear up the ambiguity of the assignment to the peak labeled *E* in Fig. 1. Eberhardt *et al.* labeled it as $(4\sigma)^{-1}(5\sigma)^{-1}(2\pi)^{+1}$ or $(5\sigma)^{-1}(1\pi)^{-1}(2\pi)^{+1}$, where in our study the latter configuration shows up as a well-defined shoulder to the former peak and is separated by approximately 2 eV.

Now focusing on the radiative decay spectra, the relative spectral intensity was calculated using a standard Lorentz line shape [17]. The intensities for all the possible ion states are then summed and plotted with respect to the excitation energy in Fig. 2. The strongest of the three peaks in our spectrum is the radiative transition back to the ground state at about 287.5 eV, which was shifted by +7.15 eV to match in energy the peak Pettersson *et al.* [18] attributed to this transition (note our core-hole peak energy is given in Table I as 287.04 eV). The following two peaks at 279.3 and 277.4 eV are from the $(5\sigma)^{-1}(1\pi)^{-1}(2\pi)^{+2}$ and $(1\pi)^{-1}(2\pi)^{+1}$ transitions, respectively. The other transitions listed in Table IV, all with decay widths below 0.1 eV, do not contribute significantly to the spectrum in this energy range. Note in Fig. 2 that the peaks in the 277–280 eV range are surrounded by the rather broad C $1s$-1π peak in the experimental spectrum. While the two peaks found in this calculation obviously contribute to the experimentally manifested structure around 280 eV, they are not the sole contributors. We must note that the experimental emission spectrum is the result of a multitude of different decay transitions from numerous different states within the experimental excitation energy range 8–10 keV.

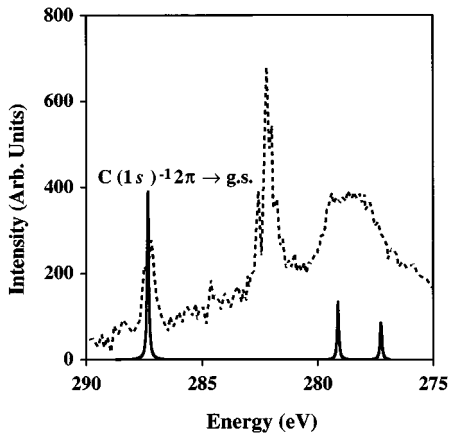

FIG. 2. Carbon 1*s* radiative decay spectrum. Carbon x-ray emission spectrum from Petterson *et al.* [18], ----, and this study, —.

C. Photoabsorption spectrum

Deexcitation electron spectroscopy is the measurement of the kinetic-energy distribution of electrons released in the decay of an excited state of a molecule. One important example occurs when a photon is absorbed, exciting an electron from a core orbital to a bound excited orbital. The subsequent decay of this intermediate state to a final state is usually thought of as a second distinct step, as shown by.

$$\begin{aligned} A &\xrightarrow{h\nu} A^* \quad \text{(step 1)}, \\ A^* &\rightarrow A^+ + e^- \quad \text{(step 2)}. \end{aligned} \tag{17}$$

In the case of long-lived intermediates, the population of the intermediate state is governed primarily by the Franck-Condon factors that are determined from the overlap integral between the initial (A) and intermediate (A^*) state. The second step, during which the intermediate decays, is effectively independent of the excitation step, once again relying on the Franck-Condon factors from the overlap between the intermediate (A^*) and final (A^+) states. However, in our case the intermediate is a short-lived C $1s\rightarrow 2\pi^*$ core-hole excited state where the decay time of this state is expected to be on the order of a few femtoseconds. In cases such as this, where the decay time is on the order of the vibrational frequency of the molecule, the two-step approximation breaks down.

When the decay widths are on the order of the vibrational spacing in the intermediate, both constructive and destructive interference occurs and must be taken into account in the description of the vibrational intensity. Theoretically, this has been accomplished by a number of means, ranging from a more sophisticated method using Green's functions [19] to a more simplistic time-dependent Franck-Condon treatment used by other investigators [2] leading to Eq. (13) given earlier.

As mentioned above, the decay of the vibrational manifold of the C $1s\rightarrow 2\pi^*$ state of CO into the valence-hole ionic continuum has been discussed in detail previously by many authors [2,13,19,20]. Experimental technique has improved to the point that Osborne *et al.* [1] were able to investigate the vibrationally resolved electronic autoionization of the core-hole resonance in CO. Their study employed a technique called mirror shadowing, allowing them to improve the resolution of their plane grating monochromator to excitation linewidths as low as 45 meV. The CO $1s\rightarrow 2\pi^*$ ion yield spectrum used for our comparison was taken with an excitation linewidth of 56 meV. The final Lorentzian linewidth obtained by deconvoluting the ion yield spectrum was found to be 86 meV.

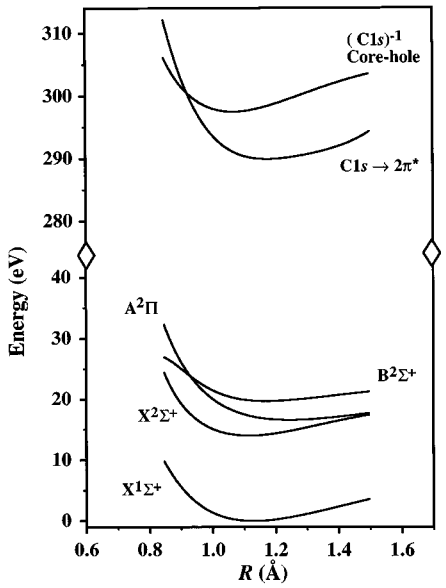

FIG. 3. Potential-energy diagram for CO, including the computed C $1s \rightarrow 2\pi^*$ resonance state, the core-hole state, as well as the ground state and three excited-state RKR potentials.

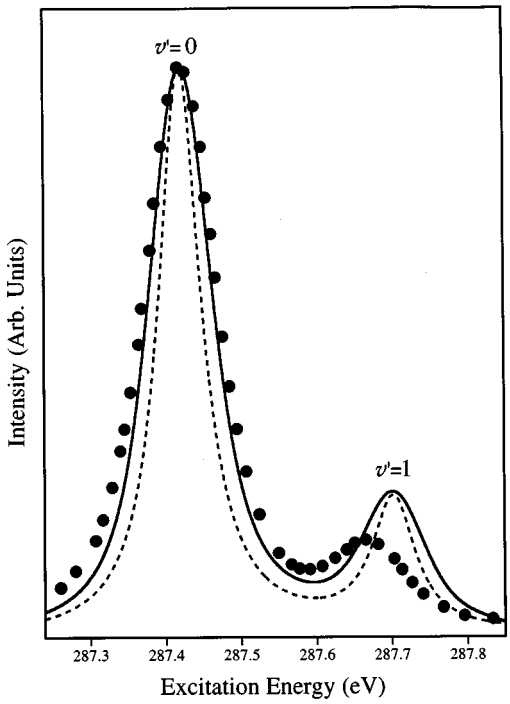

FIG. 4. CO photoabsorption spectrum. Experimental photoabsorption spectrum from Osborne *et al.* [1], ● ● ● ●; this study, ----; and convoluted with a Gaussian line profile of 56 meV, —.

We have simulated the absorption spectrum of Osborne *et al.* using Eq. (13). The Frank-Condon factors used in the vibrational intensity formula were obtained with the use of expanded Morse potential curves. For the ground state and the $A\ ^2\Pi$, $X\ ^2\Sigma^+$, and $B\ ^2\Sigma^+$ final states of CO^+, known Rydberg-Klein-Reese (RKR) potentials [21] were used and fitted to an expanded Morse curve in the form of

$$V = hcD_e\{1-e^{-a(R-R_e)}\}^2 + C_1\{1-e^{-a(R-R_e)}\}^3 + C_2\{1-e^{-a(R-R_e)}\}^4 + \cdots \quad (18)$$

for the purpose of determining the wave functions. The wave functions for the first six vibrational states were obtained from the Numerov method [22].

By calculating the cross sections for the most significant channel leading to the $^2\Pi$ state at an ionization potential of 22.6 eV as given in Table II, at various internuclear distances R ranging from 1.0 to 1.2 Å, we were able to construct the C $1s \rightarrow 2\pi^*$ core-hole and resonant potential. For each value of R a new resonance peak was obtained. The intensities of these peaks and their widths remained relatively constant with respect to change in R. The final energy values used for the resonance and core-hole potentials were obtained by computing the following series of energy differences. First we calculated the energy difference between core-hole $(\mathrm{C}\ 1s)^{-1}$ state and resonance C $1s \rightarrow 2\pi^*$ state at various values of R using the single-center scattering code as described above. We then calculated the energy difference between the core-hole state and $X\ ^1\Sigma^+$ initial state using the GAMESS-UK program. These two energy differences were added to the experimentally determined RKR $X\ ^1\Sigma^+$ initial-state potentials to obtain a potential for the core-hole and resonance state. Figure 3 displays the resulting resonance state potential as well as the initial- and final-state RKR potentials. The vibrational wave functions of the resonance state potential-energy curve were subsequently obtained in an analogous manner to vibrational states of the initial- and final-state potentials.

The final Frank-Condon overlap integrals used in the spectral intensity formula given in Eq. (13) were obtained from the normalized initial, final, and resonance wave functions. The calculated intensities for the individual final states were then weighted according to the calculated individual spectral widths and then summed. However, in comparing the theoretically obtained absorption spectrum with the experimental photoabsorption spectrum for the C $1s \rightarrow 2\pi^*$ obtained by Osborne *et al.* [1] note that while there is relatively good agreement in the relative peak positions, the FWHM of the calculated spectrum of 64 meV is approximately one-half of the observed value of 112 meV. In Table V note that a width of 86 meV for Osborne *et al.* is reported. This value for the width comes from deconvoluting the observed spectrum into the monochromator Gaussian line profile and the natural Lorentzian linewidth. To obtain a better representation of the observed spectrum we then convoluted our intensity spectrum with the Gaussian line profile of Osborne *et al.* of 56 meV. The final theoretically obtained spectrum is given in Fig. 4 as a solid line. Note that the FWHM of this peak is now 101 meV, much closer to the experimentally obtained spectrum of Osborne *et al.* The theoretical background of deconvoluting the Gaussian statistical and natural Lorentzian line shapes from an experimental spectrum is covered in detail by Wertheim *et al.* [23]. We have shifted the energy scale and the intensity so that the peak of the experimental and theoretical curves agree at a photon energy of 287.4 eV. This corresponds to an energy shift of −2.72 eV. Concentrating on Fig. 4 we note that the experimental peak maximum for the $v' = 1$ transition appears

TABLE VII. Experimental and calculated vibrational energies for the absorption spectrum.

	Experimental[a]		Calculated	
v'	Relative intensity	Energy (eV)	Relative intensity	Energy (eV)
0	1.000	287.410	1.000	287.41[b]
1	0.130	287.659	0.255	287.68
2	0.018	287.909	0.004	287.95

[a]Reference [1].
[b]Shifted to agree with experiment.

slightly redshifted relative to the theoretical peak. This is the result of the overlapping of the wider experimental peaks and a small difference in position of the underlying peaks as given in Table VII. The discrepancy between our theoretical simulation and the experimental spectrum is due to the sensitivity of this peak to shifting the minimum of the resonance state to different values. The minimum of the resonant potential was found to lie at 1.1629 Å, in comparison to 1.1529 Å reported by Neeb *et al.* [8]. This difference of 0.01 Å then leads to the difference in the absorption spectra seen in Fig. 4. In Table VII we have compared the calculated vibrational energies for the absorption spectrum with our calculated values.

V. CONCLUSION

The aim of the present work was to demonstrate by means of a few numerical techniques the ability to simulate theoretically the absorption and the subsequent radiative and nonradiative decay from the extremely short-lived C $1s \rightarrow 2\pi^*$ core-hole resonance state of carbon monoxide. After the initial calculation of the core-hole and resonance state cross sections utilizing the multichannel Schwinger approach, we utilized Fano's line profile to compute the spectral widths for the multitude of nonradiative decay channels from the resonance state. This study shows that it is not necessary to perform a large multichannel calculation with all the possible decay channels, but rather that a series of smaller two-channel calculations is sufficient to obtain an accurate total decay width from the intermediate state. This study also utilized these partial decay widths to calculate the transition rates for the nonradiative decay resulting in a simulated deexcitation spectrum that provided excellent agreement with the experimental data. Also, the transition moments from the multichannel Schwinger calculations were used in the calculation of the radiative decay lifetime and in the simulation of a radiative decay spectrum of the resonance state. We have shown that this approach successfully reproduces the main features of the experimental spectra.

Comparing, the nonradiative lifetime of our core-hole resonance state on the order of 10^{-13} s to the characteristic molecular vibrational frequency of CO, which is in the range 10^{13}–10^{14} s^{-1}, it is easy to understand why it was necessary to take into consideration the local vibrational interference effects in the absorption spectra. The application of this well-known lifetime vibrational interference formula to the core-hole decay of carbon monoxide has proven to provide excellent correlation with experimental studies, as shown in the comparison with the work of Osborne *et al.* in Fig. 3.

ACKNOWLEDGMENTS

We acknowledge partial support from the Robert A. Welch Foundation (Houston) under Grant No. A-1020 and also the helpful discussions with Robert Zurales.

[1] S. J. Osborne, A. Ausmees, S. Svensson, A. Kivimäki, O.-P. Sairanen, A. Naves de Brito, H. Aksela, and S. Aksela, J. Chem. Phys. **102**, 7137 (1995).
[2] A. Flores-Riveros, N. Carreia, H. Ågren, L. Pettersson, M. Bäckström, and J. Nordgren, J. Chem. Phys. **83**, 2053 (1985).
[3] K. J. Randall, A. L. D. Kilcoyne, H. M. Köppe, J. Feldaus, A. M. Bradshaw, J.-E. Rubensson, W. Eberhardt, Z. Xu, P. D. Johnson, and Y. Ma, Phys. Rev. Lett. **71**, 1156 (1993).
[4] R. R. Lucchese and V. McKoy, Phys. Rev. A **28**, 1382 (1983).
[5] R. R. Lucchese, K. Takatsuka, and V. McKoy, Phys. Rep. **131**, 147 (1986).
[6] R. Lucchese, Phys. Rev. A **33**, 1626 (1986).
[7] R. R. Lucchese, J. Chem. Phys. **92**, 4203 (1990).
[8] M. Neeb, J. Rubensson, M. Biermann, and W. Eberhardt, J. Electron Spectrosc. Relat. Phenom. **67**, 261 (1994).
[9] G. Bandarage and R. R. Lucchese, Phys. Rev. A **47**, 1989 (1993).
[10] U. Fano, Phys. Rev. **124**, 1866 (1961).
[11] R. E. Stratman and R. R. Lucchese, J. Chem. Phys. **102**, 8493 (1995).
[12] M. F. Guest and P. Sherwood, *GAMESS-UK* (SERC Daresbury Laboratory, Daresbury, 1992).
[13] N. Correia, A. Flores-Riveros, H. Ågren, K. Helenelund, L. Asplund, and U. Gelius, J. Chem. Phys. **83**, 2035 (1985).
[14] T. H. Dunning and J. P. Hay, in *Methods of Electronic Structure Theory*, edited by H. F. Schaefer III (Plenum, New York, 1977), p. 1.
[15] R. E. Stratman, R. W. Zurales, and R. R. Lucchese, J. Chem. Phys. **104**, 8989 (1996).
[16] W. Eberhardt, E. W. Plummer, C. T. Chen, and W. K. Ford, Aust. J. Phys. **39**, 853 (1986).
[17] R. Karazija, *Introduction to the Theory of X-Ray and Electronic Spectra of Free Atoms* (Plenum, New York, 1996).
[18] L. Pettersson, N. Wassdahl, M. Bäckström, J. E. Rubensson, and J. Nordgren, J. Phys. B **18**, L125 (1985).
[19] F. K. Gel'mukanov, L. N. Mazalov, and A. V. Kondratenko,

Chem. Phys. Lett. **46**, 133 (1977).
[20] F. Kaspar, W. Domcke, and L. S. Cederbaum, Chem. Phys. **44**, 33 (1979).
[21] P. H. Krupenie and S. Weissman, J. Chem. Phys. **43**, 1529 (1965).
[22] W. H. Press, B. P. Flannery, S. A. Teukolsky, and W. T. Vetterling, *Numerical Recipes: The Art of Scientific Computing* (Cambridge University Press, New York, 1988).
[23] G. K. Wertheim, M. A. Butler, K. W. West, and D. N. Buchanan, Rev. Sci. Instrum. **45**, 1369 (1974).
[24] D. A. Shaw, G. C. King, D. Cvejanovic, and F. H. Read, J. Phys. B **17**, 2091 (1984).